Applied Surface Science 464 (2019) 692–699

Contents lists available at ScienceDirect

Applied Surface Science

journal homepage: www.elsevier.com/locate/apsusc

Full Length Article

Towards carbon monoxide sensors based on europium doped cerium dioxide

P.P. Ortega[a,*], L.S.R. Rocha[a], J.A. Cortés[a], M.A. Ramirez[a], C. Buono[b], M.A. Ponce[b], A.Z. Simões[a]

[a] São Paulo State University (UNESP) – School of Engineering of Guaratinguetá, Av. Dr. Ariberto Pereira da Cunha 333, Portal das Colinas, 12.516-410, Guaratinguetá, São Paulo, Brazil

[b] University of Mar del Plata (UNMdP), Institute of Materials Science and Technology (INTEMA), National Research Council (CONICET), Av. Juan B. Justo 4302, 7600 Mar del Plata, Argentina

ARTICLE INFO

Keywords:
Cerium dioxide
Thick films
Gas sensor
Carbon monoxide

ABSTRACT

$Ce_{1-(3/4)x}Eu_xO_2$ (x = 0.00 and x = 0.08) thick films were prepared from nanoparticles synthesized by the microwave-assisted hydrothermal route, aiming their application as a carbon monoxide sensing material to prevent deaths caused by this highly toxic gas. XRD analysis revealed that the nanopowders are free from secondary phases and crystallize in the fluorite cubic structure, which is confirmed by Raman spectroscopy. The Eu-doped ceria film presented much higher response (S) values than pure ceria, demonstrating the higher sensitivity of the doped system to carbon monoxide, especially at 400 °C. Electrical measurements under different atmospheres revealed a remarkably fast carbon monoxide response time for the Eu-doped film when compared with the pure sample, proving that the introduction of europium cations in the ceria lattice as dopants has a positive effect on the carbon monoxide sensing properties.

1. Introduction

Cerium dioxide (CeO_2), also known as ceria, is a non-stoichiometric type-n semiconductor of great technological interest, which has been widely applied in multiple fields due to its remarkable properties [1–8]. Among the several methods to synthesize CeO_2 nanostructures that have been reported [9–20], the hydrothermal synthesis [10] stands out as a practical and useful technique to obtain high quality nanostructures of metal oxides, since it provides good control over homogeneity, particle size, chemical composition, phase formation and morphology of the resultant products [21]. The use of microwaves as the heating mechanism in the hydrothermal technique, opposed to the conventional method [21–26], has been described as a more environmentally friendly technique to synthesize ceramic nanostructures with lower temperature, lower power consumption and significant shorter time [8,22,27–29].

Ceria crystallizes in a fluorite structure with space group Fm3m and lattice parameter of 5.411 Å [30], where the cerium atoms are packed in a face centered cubic cell with oxygen atoms occupying tetrahedral sites. Alongside other rare-earth elements, cerium has unique properties due to an unfilled 4f orbital. Most applications are related to its Oxygen Storage Capacity (OSC), i.e. the ability to absorb or release oxygen, which is a result of cerium easy transition between oxidation states (Ce^{4+}/Ce^{3+}). During CeO_2 reduction, an oxygen vacancy is created together with the localization of an electron in a Ce 4f orbital [31]. This process is explained by the Kröger-Vink notation as follows:

$$O_o^x + 2\ Ce_{Ce}^x \leftrightarrow V_o^{\cdot\cdot} + 2\ Ce_{Ce}' + \tfrac{1}{2}\ O_{2(g)} \quad (1)$$

In order to maintain charge neutrality, a positive charged oxygen vacancy ($Vo^{\cdot\cdot}$) is created to compensate the negative effective charge generated after cerium reduction ($2Ce_{Ce}'$), resulting in a non-stoichiometric compound (CeO_{2-x}). Therefore, an increase in oxygen vacancy concentration is expected when doping ceria with lower oxidation state cations. Accordingly, rare-earth elements (mostly trivalent cations, such as La^{3+}, Gd^{3+}, $Eu^{3+/2+}$ and Sm^{3+}) have been extensively applied as ceria dopants due to their property similarity and the possibility of forming solid solutions, improving its activity, selectivity and thermal stability [32]. Also, the higher number of oxygen vacancies in the lattice promoted by rare-earth doping increases the conductivity and OSC, making it particularly interesting for gas sensing applications.

Carbon monoxide (CO) is a colorless, odorless and extremely toxic life-threating gas known as the “Silent Killer”, due to its undetectable presence in the environment by humans. Therefore, a reliable and efficient CO sensor is needed to alert and protect potential victims from this threat. Gas sensor devices must not only have high sensitivity, stability, reversibility and selectivity, but also low cost and low energy consumption [33]. Fast response, reduced dimensions, portability and real time detection are other important parameters that must be considered [34]. Control over particle size and morphology plays a

* Corresponding author.
E-mail address: pedro.ortega@hotmail.com.br (P.P. Ortega).

https://doi.org/10.1016/j.apsusc.2018.09.142
Received 12 June 2018; Accepted 17 September 2018
Available online 18 September 2018

significant role when it comes to improving sensitivity. Particles with reduced size distribution lead to a higher surface-CO interaction and also allow the sensor to operate at lower temperatures and consume less energy [21,26]. Other important parameters that affect sensitivity are composition, surface modification, temperature, humidity and microstructure [26].

The sensing mechanism in polycrystalline semiconductors is related to chemical reactions on the surface of the semiconductor when exposed to the target gas (e.g. carbon monoxide). The oxygen present in the atmosphere adsorbs on the surface and forms anionic oxygen (O^-) by capturing electrons from the conduction band [35,36]. These electrons are then trapped by the oxygen species at the surface, creating an electron-depleted region and consequently decreasing the conductivity of the sensor. Subsequently, the exposure to the target gas promotes the oxidation of CO molecules by the adsorbed O^- to form carbon dioxide (CO_2). The previously trapped electron then returns to the conduction band, which is followed by an increase in the conductivity [26,34,37]. Thus, the response of the sensor is measured by means of the electrical signal associated with variations in the conductivity during semiconductor-target gas interaction.

In previous work, we put great effort into characterizing and optimizing the preparation of pure and doped CeO_2 thick films with nanostructures synthesized by the MAH method [27,29,38–40]. In this paper, we discuss the preparation and characterization of pure and europium-doped CeO_2 thick films from the nanoparticles synthesized by the microwave-assisted hydrothermal method. The main goal is to evaluate their response as a CO sensing material and link this response to the microstructural modifications induced by europium doping.

2. Experimental procedure

2.1. Synthesis of the ceramic nanopowder

Nanopowders of $Ce_{1-(3/4)x}Eu_xO_2$ (x = 0.00 and x = 0.08) were synthesized via microwave-assisted hydrothermal route. Ammonium cerium(IV) nitrate ($Ce(NH_4)_2(NO_3)_6$) and europium(III) oxide (Eu_2O_3) were used as precursors, both provided by Sigma-Aldrich with 99.0 and 99.9% purity, respectively. The cerium precursor was dissolved in aqueous media at 80 °C under constant magnetic stirring. In parallel, the europium oxide was dissolved under the same conditions, except for the addition of nitric acid (HNO_3 65%, Synth) to assist with the dissolution process, and then added to the cerium solution. A 2 mol·L^{-1} potassium hydroxide solution (KOH 99.5%, Synth) was slowly added to the mixture at room temperature to adjust the pH to a value of 10. Subsequently, the mixture was transferred to a sealed Teflon autoclave and placed in a hydrothermal microwave oven (2.45 GHz, 800 W). The reactional system was heat treated at 100 °C for 8 min, with a heating rate of 10 °C/min, which are optimized parameters [38]. The resultant solution was transferred to centrifuge tubes, being then submitted to three cycles of washing with deionized water at 2000 rpm for 10 min each. Afterwards, the obtained $Ce_{0.94}Eu_{0.08}O_2$ nanoparticles were dried at 100 °C for 48 h in an oven.

The obtained nanostructures were characterized by X-ray powder diffraction (XRD) using a Rigaku-DMax/2500PC with Cu-Kα radiation (λ = 1.5406 Å) in the 2θ range from 20 to 80° with 0.2°/min. The Rietveld refinement was made with the software Topas 4.2. The Raman spectroscopy characterization was obtained by a LabRAM iHR550 Horiba Jobin Yvon spectrometer with a 514 nm wavelength laser as excitation source and spectral resolution of 1 cm^{-1}, with 40 scans in the range of 100–1500 cm^{-1}, coupled to a CCD detector. The procedure was made with an Argon-ion laser, whose wavelength is 514.5 nm and with a power of 8 mW. Ultraviolet–visible (UV–vis) spectroscopy for the optical absorbance spectra was taken using a Cary 5G (Varian, USA) spectrophotometer in diffuse reflection mode and the band gap energy was obtained by means of the Tauc's method, which is based on the relationship between diffuse reflectance and band gap given by the following equation:

$$(h\nu\alpha)^{1/n} = A(h\nu - E_g) \quad (2)$$

where α is the absorption coeficiente, hν is the photon energy, A is a constant and E_g is the band gap. The n value depends on the nature of the electronic transitions: direct allowed (n = 1/2), direct forbidden (n = 3/2), indirect allowed (n = 2) and indirect forbidden (n = 3). Therefore, considering direct allowed transition, the equation is:

$$(h\nu\alpha)^2 = A(h\nu - E_g) \quad (3)$$

The plot of $(h\nu\alpha)^2$ in function of hν is known as the Tauc plot. The extrapolation of the linear portions of the curves until it intersects the axis where absorption is zero gives the band gap energy. The high resolution transmission electron microscopy (HRTEM) images were taken at room temperature by dispersing the nanoparticles obtained by the MAH method in ethanol and, after drying, adding them to a 300 mesh copper grade, followed by ultrasonic vibration for 5 min. The microscope used was a FEI TECNAI F20.

2.2. Preparation of the films

A paste, based on a mixture of the nanopowder obtained from the MAH synthesis and an organic binder (glycerol), was used to prepare thick porous films by the screen-printing technique onto 96% dense insulating alumina substrates, on which a 25 nm titanium (Ti) adhesion layer and a 200 nm platinum layer had been deposited by RF-Sputtering. The interdigitated platinum (Pt) electrodes were delineated by a home-built micromachining laser. The substrate dimensions are 20 × 10 mm (length × width) and the Pt electrodes have a resistance of 10 Ω. The powder/binder ratio used was 1.6 g/ml. After deposition, the films were heat treated in dry air atmosphere with 1 °C/min steps up to 380 °C and maintained in this temperature for 2 h, in order to evaporate the binder. An illustration of the deposited film is shown in Fig. 1.

The surface morphology of the film was observed using a high-resolution field-emission gun scanning electron microscope (FEG-SEM) Supra 35-VP (Carl Zeiss, Germany). The film thickness was measured with a Surtronic 3+ (Taylor Hobson) profilometer with a diamond stylus (radius: 1 μm) and the cross section was analyzed using SEM microscopy. The electrical resistance measurements were carried out in function of time (at 400 °C) and temperature, in vacuum, dry air and CO atmospheres at a constant pressure of 100 mmHg. The electrical measurements were made in a optoelectronic device (Patent INPI Argentina 201501039539/INPI Brazil 10 2016 028383 3 [41,42]) consisting of a closed chamber in which three cycles of heating in vacuum up to 380 °C were made before measuring the resistance values, assuring the volatilization of any humidity. The measurements were made when the samples got to a steady state and no changes in resistance over time were observed, with an applied magnitude of excitation current of 1 mA, obtained using the two-wire technique with a DC-type measurement. An Agilent 3440A multimeter was used for the electrical resistance measurements.

3. Results and discussion

3.1. Characterization of the nanoparticles

In order to confirm the formation of a Ce-Eu solid solution, X-Ray Diffraction (XRD) analysis of the crystalline phases was carried out (Fig. 2). The XRD patterns for both pure and europium doped ceria show all the characteristic peaks of the CeO_2 fluorite structure (JCPDS 34-0390) [27] and no peaks of any other phase were detected. The absence of diffraction peaks belonging to Eu_2O_3 phase indicates the isomorphic substitution of cerium by europium cations in the lattice and/or that it might be present in a highly dispersed state [32]. A small shift of diffraction peaks towards lower angles can be observed in the

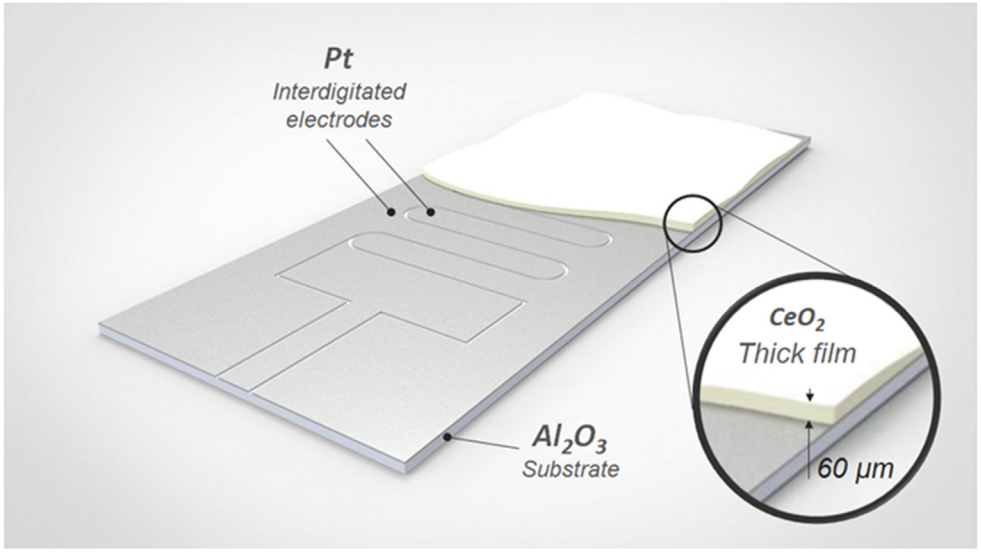

Fig. 1. Illustration of the deposited ceria film on alumina substrates with interdigitated Pt electrodes.

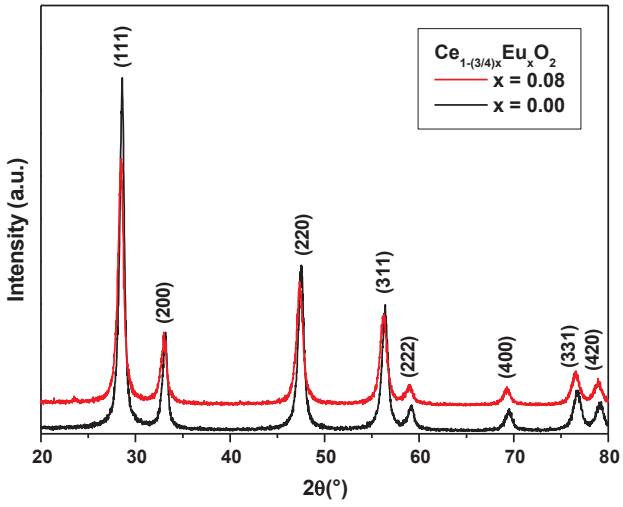

Fig. 2. XRD pattern of pure and europium doped cerium dioxide nanoparticles synthesized at 100 °C for 8 min by the MAH method under KOH mineralizer.

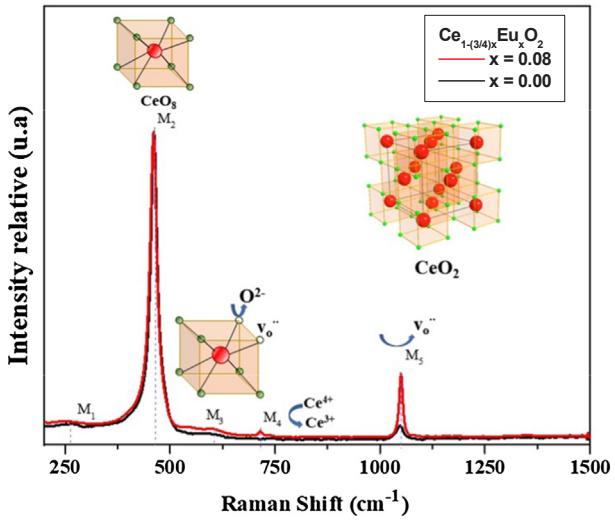

Fig. 3. Raman spectra of pure and europium doped cerium dioxide nanoparticles synthesized at 100 °C for 8 min by the MAH method under KOH mineralizer.

europium doped sample when compared to pure ceria, a fact explained by the replacement of cerium with europium cations in the lattice. Since Eu^{3+} (1.066 Å) cations are larger than Ce^{4+} (0.97 Å), it causes an enlargement of octahedral sites in the fluorite structure, resulting in the shift of the peaks [43]. The lattice parameter for the pure sample was 5.412 Å, which is compatible with the theoretical value for CeO_2 found in the literature [27]. The addition of Eu^{3+} produces a small increase in the lattice parameter and it is also a consequence of the difference between the ionic radii of the cerium and europium cations [44]. The Rietveld refinement shows that the europium cations enter in the Ce^{4+} and Ce^{3+} sites, due to the ceria non-stoichiometry. A close inspection of the refinement parameters (R_{wp}, R_e, GoF) presented in Table 1 indicates that the refinement is coherent.

Fig. 3 shows the Raman spectra of the samples. Five modes (M_1-M_5) can be seen in the plot. The M_1 mode, close to 260 cm^{-1}, is associated to disorders in the system and it is evident for both samples. The M_2 mode at 465 cm^{-1} is assigned to the F_{2g} symmetric vibration mode associated to the cubic fluorite structure of ceria [43]. This triply degenerate Raman mode is related to the [CeO_8] unit and can be seen as a symmetric breathing mode of oxygen atoms around the cerium cation [45–47]. The M_3 and M_5 modes are attributed to the higher concentration of oxygen vacancies and the expansion-contraction of the oxide lattice as a consequence of the introduction of europium cations [27], which can also be noted with the M_4 mode. The absence of Raman modes of the doping oxide Eu_2O_3 is another evidence of the formation

Table 1
Rietveld refinement data for the pure and europium doped samples.

Sample	Lattice parameter (a = b = c) Å	R_{exp}	R_p	R_{wp}	GoF	R-Bragg	Stoichiometry
CeO_2	5.412	10.49	7.47	11.52	1.10	1.56	CeO_2
$Ce_{1-(3/4)x}Eu_xO_2$ in Ce^{3+}	5.418	11.31	8.13	12.43	1.10	1.25	$Ce_{0.97}Eu_{0.03}O_2$
$Ce_{1-(3/4)x}Eu_xO_2$ in Ce^{4+}	5.417	11.31	8.15	12.44	1.10	1.36	$Ce_{0.95}Eu_{0.05}O_3$

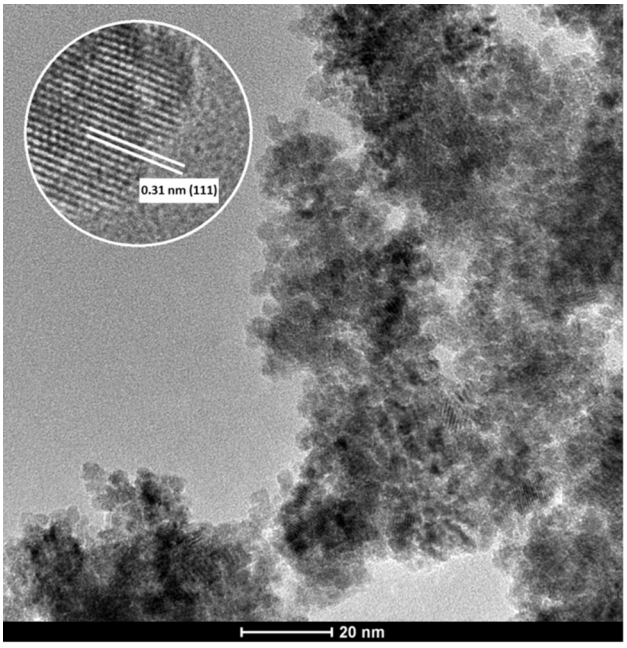

(a)

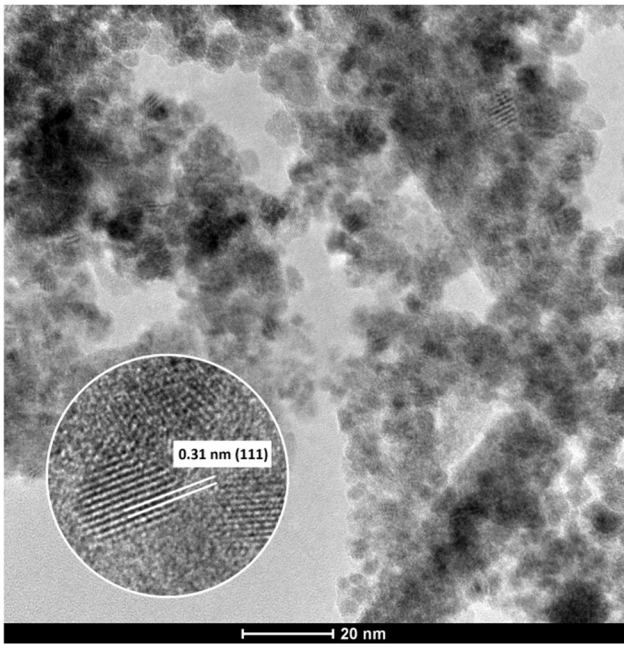

(b)

Fig. 4. HRTEM images of the pure (a) and europium doped (b) cerium dioxide nanoparticles synthesized at 100 °C for 8 min by the MAH method under KOH mineralizer.

of a solid solution, as shown by XRD analysis.

Fig. 4 illustrates the images obtained by high resolution transmission electronic microscopy (HRTEM) of the nanoparticles synthesized by MAH. The nanoparticles are homogenously distributed and have a rounded shape, with an average size of 4 nm. At the beginning of the synthesis, multiple nucleation sites are formed in the solution. As the reaction goes on in a highly diluted solution, there are not enough reactants left for the crystal growth. Therefore, the nanoparticles have an extremely fine size distribution [27]. Also, a strong tendency to form agglomerates was observed, which can be explained by the influence of Van der Waals forces on the nanoparticles. The interplanar spacing of 0.31 nm is related to the crystallographic plane (1 1 1) of the ceria

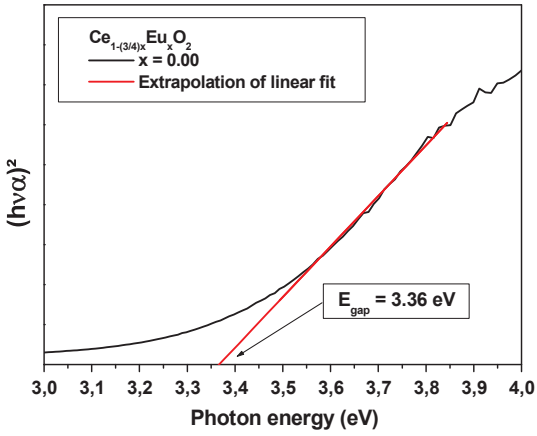

(a)

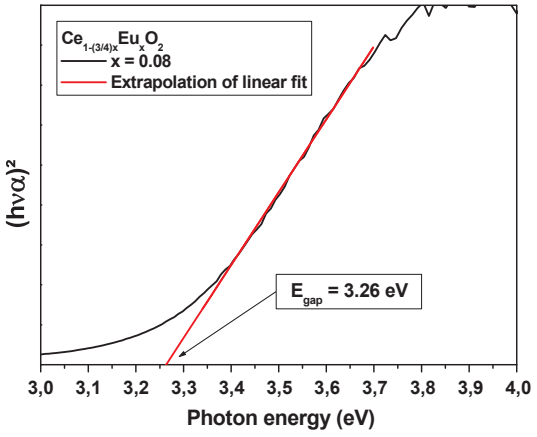

(b)

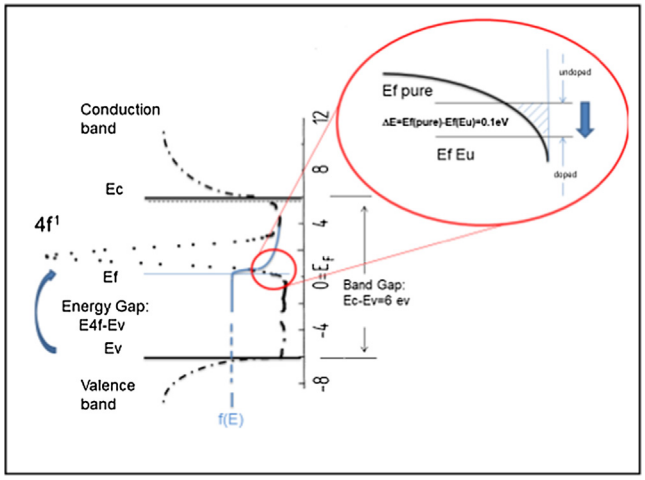

(c)

Fig. 5. UV–Vis analysis of pure (a) and europium doped (b) cerium dioxide nanoparticles synthesized at 100 °C for 8 min by the MAH method under KOH mineralizer and (c) band gap diagram of ceria showing the E_F movement after Eu doping and the energy gap.

structure, in agreement with the JCPDS 34–0390 file and the XRD data.

Fig. 5 shows the Tauc plots for the samples and their respective energy gaps. Cerium dioxide is a poor ionic conductor with a wide band gap (E_g) of 6 eV [48], with oxygen vacancies ($V_O^{\cdot\cdot}$) as the predominant ionic defect. This is the theoretical value and it is associated with electronic transitions between oxygen 2p and cerium 5d states.

However, the experimental band gap values are lower than 6 eV, as shown in Fig. 5. The band gap represents the energy required for the excitation of one electron from the highest energetic level of the valence band to the lowest energetic level of the conduction band, thereby increasing its conductivity. In ceria, the electrons are localized in the 4f states instead of the conduction band, therefore we shall call energy gap the energy required for the excitation of one electron from the highest energetic level of the valence band to the 4f states. The E_g of 3.36 eV (Fig. 5a) is close to what has been reported in the literature for pure ceria [49]. Such energy gap value is due to the existence of intermediate transitions between oxygen 2p states and cerium empty 4f states. Cerium reduction from Ce^{4+} to Ce^{3+} and the consequent formation of oxygen vacancies create an intermediate state within the band gap (near the conduction band, represented with dots in Fig. 5c). During reduction, an electron is localized in cerium 4f state, previously empty, making it easier the transition between cerium 4f and 5d states [49–50]. Therefore, the introduction of a trivalent cation (Eu^{3+}) in the lattice is expected to promote a higher number of oxygen vacancies and also have a narrowing effect on the band gap. As can be seen in Fig. 5b, Eu-doped ceria presented a slightly lower energy gap value of 3.26 eV. The band gap diagram showing the E_F movement after Eu doping is shown in Fig. 5c. In this band diagram, a reduction in the number of states available for $4f^1$ electrons is shown. This E_F movement (decrease, in 0.1 eV) increases the Eu-doped films resistance.

3.2. Characterization of the thick films

The images of the films prepared from the pure and Eu-doped nanoparticles obtained by the MAH route are shown in Fig. 6a and 6b, respectively, along with the cross-section view. The FEG-SEM image shows that the nanoparticles have a tendency to form large agglomerates, probably due to the Van der Waals forces arising from O-H groups present in both the precursor solution and the binder (glycerol) [27,40]. In the hydrothermal process, the presence of alkaline medium is essential. The “dissolution and crystallization” process can be utilized to describe the reactions [51]. During the hydrothermal treatment, Ce^{3+} and Eu^{3+} hydroxides undergo an attack of KOH to dissolve and react at high temperatures and pressures, and then precipitate as insoluble ceramic oxide nanoparticles from the supersaturated hydrothermal fluid. Therefore, the dissolution and crystallization process continues in the supersaturated fluid in such a way that the system is self-stabilizing. To reduce the surface energy, the primary particles have a tendency to form nearly spherical agglomerates, in a minimum surface to volume ratio and hence reducing surface free energy. The cross-section view of the pure and doped thick films shows an average thickness of 45 and 55 μm, respectively.

In order to explain the electrical behavior of our samples, these previously reported results were taken into account:

I. Rare-earth oxides with 4f-shells of the lanthanide ions are likely to present narrow bands and then the electrical conduction would involve 4f electrons that migrate by an activated hopping mechanism [52].
II. The mechanism of conduction in these oxides can be understood in terms of the hopping model and the small polaron theory. Fully ionized oxygen vacancies seem to be the predominant defect contributing to the defect structure in our samples [53].
III. Small polaron is a defect created when an electronic carrier becomes trapped at a given site as a consequence of the displacement of adjacent atoms or ions. The entire defect (carrier plus distortion) then migrates by an activated hopping mechanism. Small polaron formation can take place in materials whose conduction electrons belong to incomplete inner (d or f) shells which, due to small electron overlap, tend to form extremely narrow bands [52].

To analyze the electrical behavior of the doped and undoped thick films, their responses under CO and dry air atmospheres were evaluated by means of the response time (t_{resp}) and recovery time (t_{rec}), which are two of the most important characteristics of a sensor material. The response time is defined as the period of time the material takes to reduce its resistance by 90% of the initial value when exposed to the target gas. The recovery time, on the other hand, is the amount of time necessary to recover 90% of the initial resistance after the gas exposure [54].

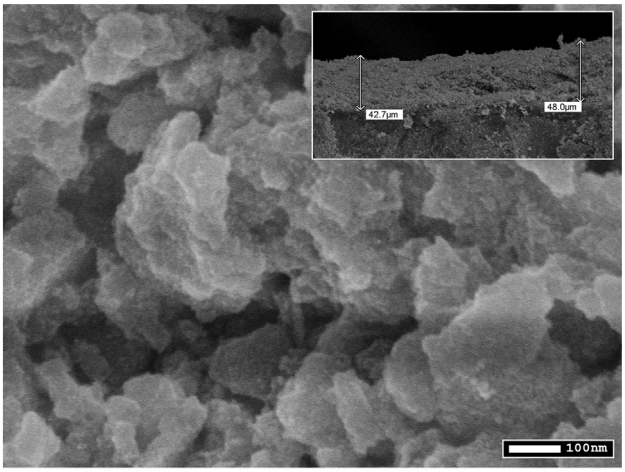

(a)

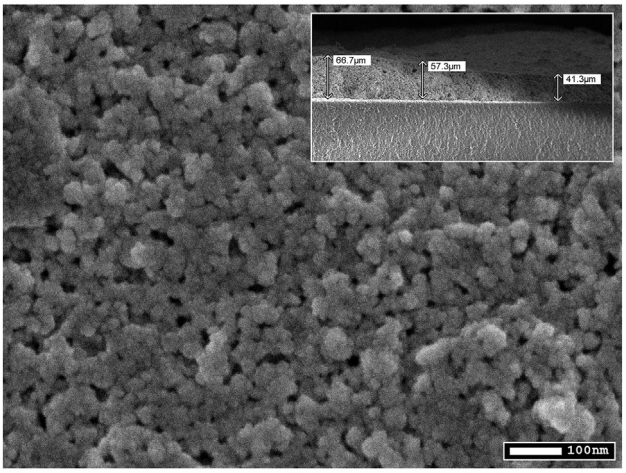

(b)

Fig. 6. FEG-SEM image of the pure (a) and europium doped (b) film surface (cross section as index) prepared from the nanoparticles synthesized at 100 °C for 8 min by the MAH method under KOH mineralizer.

The interaction between gaseous species and the sensor film can be separated in two steps. The first is related to the adsorption of oxygen onto the surface of the film, resulting in the formation of three adsorbed species that depend on the work temperature: O_2^- ($T < 100$ °C), O^- (100 °C $< T <$ 300 °C) or O^{2-} ($T >$ 300 °C) [36,55]. The second step consists in the reaction between the adsorbed oxygen species and the target gas (CO). This process is explained by the following equations [56]:

$$2CO + O_2^- \rightarrow 2CO_2 + e^- \quad (T < 100\,^\circ C) \tag{4}$$

$$CO + O^- \rightarrow CO_2 + e^- \quad (100\,^\circ C < T < 300\,^\circ C) \tag{5}$$

$$CO + O^{2-} \rightarrow CO_2 + 2e^- \quad (T > 300\,^\circ C) \tag{6}$$

Eqs. (4)–(6) show that one or two electrons are released as a product of the reaction between CO and oxygen and then they return to the conduction band of the typical semiconductor. In our samples, we must take into account the minor energy unoccupied $4f^0$ states that are the

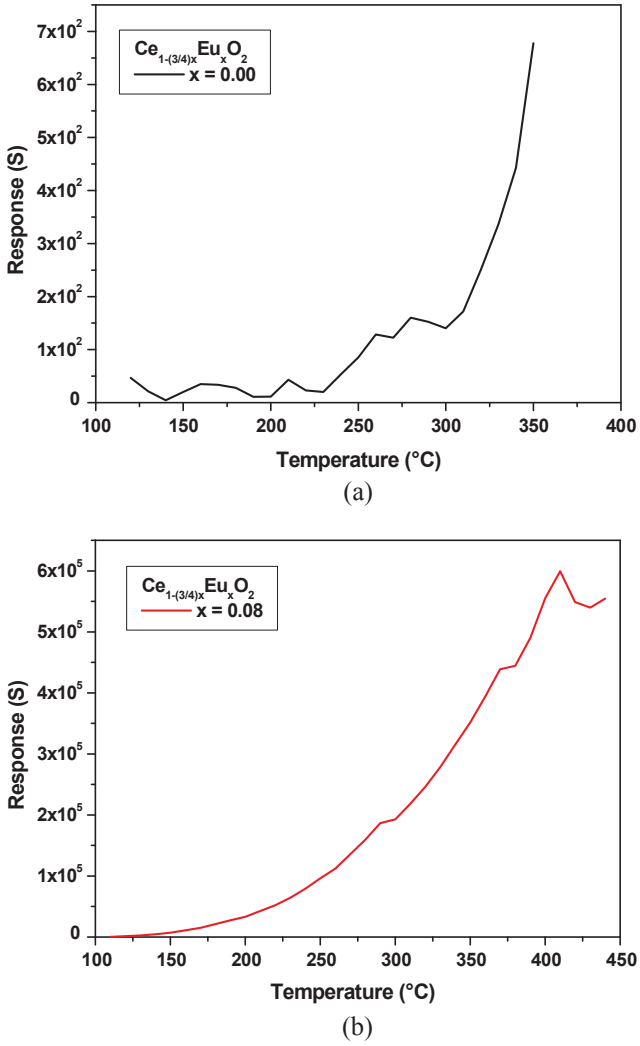

Fig. 7. Response versus temperature for the films synthesized from the nanoparticles synthesized at 100 °C for 8 min by the MAH method under KOH mineralizer.

responsible of the hopping conduction. As result of the increase in the number of electrons in $4f^0$ to $4f^1$ states, the resistance decreases during the exposure to a reducing gas.

To gain confidence on the optimum Eu-doped film work temperature, a study of the response as function of temperature was carried out. For reducing gases (such as CO), the sensor response (S) is defined as $\Delta R/R_{CO} \times 100$, where $\Delta R = (R_{air} - R_{CO})$, being R_{air} the resistance of the film in air and R_{CO} the resistance of the film when exposed to carbon monoxide [57]. Fig. 7 illustrates the response of the films as function of temperature. The response increases dramatically for temperatures above 200 °C for both pure and Eu-doped films, which can be explained by a decrease in Rco values (at this temperature range) as consequence of surface and bulk reduction from CO exposure and consequently an increase in the number of thermalized electrons in the $4f^1$ states. The doped system (Fig. 7b) presented much higher response values than pure ceria (Fig. 7a), proving to be more sensitive to carbon monoxide. This behavior is in good agreement with the results obtained at 380 °C (Fig. 8), in which the exposure to CO causes a fast and sharp decrease in the resistance, in contrast to the oxygen atmosphere, that has the opposite effect. The sensor response to CO for the Eu-doped film reaches a maximum value around 400 °C, which can be considered as the best temperature for the sensor film to operate.

Therefore, in order to assess the Eu-doped CeO_2 sensor film response to CO gas, and considering the working temperature from Fig. 7b, the

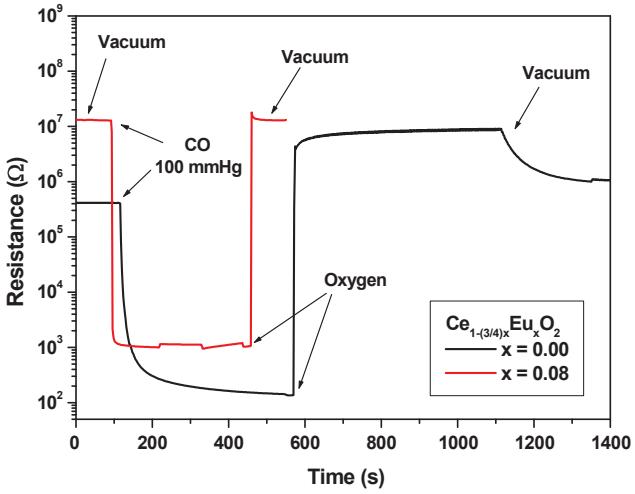

Fig. 8. Resistance in function of time and atmosphere for pure and europium doped ceria films prepared from the nanoparticles synthesized at 100 °C for 8 min by the MAH method under KOH mineralizer.

resistance was monitored in function of time under oxygen, carbon monoxide, and vacuum atmospheres at 380 °C (Fig. 8). A t_{resp} of 56 s was calculated for the pure ceria film when exposed to CO, while the Eu-doped sample presented a t_{resp} of 0.9 s. The recovery time was 3.8 and 0.5 s for pure and Eu-doped ceria, respectively. The resistance of the films increases after the exposure to oxygen. This is associated with the oxygen diffusion into the lattice, which annihilates the oxygen vacancies, reducing their concentration and the electron density. Both t_{resp} and t_{rec} obtained for the Eu-doped system are remarkable results when compared to previously reported values [57–61], proving that europium doped ceria can significantly improve the sensing properties of ceria to carbon monoxide.

Finally, in order to better understand the resistance changes with gas exposure, a band diagram, which corresponds to the electric conduction mechanism observed for pure and Eu doped samples, is shown in Fig. 9. As a consequence of the gases adsorption onto the surface, the energy difference between the Fermi level (E_F) and the 4f state (E_{4f}–E_F) changes, reducing (oxidant gases) or increasing (reductive gases) the number of electrons available for conduction. If we also consider the possible Ce^{4+} reduction to Ce^{3+} when samples are exposed to CO and the oxidation when samples are exposed to oxygen, then the number of electrons in 4f states changes drastically. Also, it can be noted that after the Eu addition into the CeO_2 lattice, the sample conductivity decreased as a consequence of the E_F decreasing in 0.1 eV, as shown by the Tauc plots in Fig. 5.

4. Conclusions

Thick films were prepared from the $Ce_{1-(3/4)x}Eu_xO_2$ (x = 0.00 and x = 0.08) nanoparticles synthesized by the microwave-assisted hydrothermal route. XRD analysis of the samples revealed the formation of a Ce-Eu solid solution with a fluorite cubic structure and no phase segregation. Raman spectroscopy did not present any mode related to impurities from the precursors or synthesis method. UV–Vis measurements show smaller band gap energies than the predicted by theoretical values, mainly due to the presence of Eu^{3+} cations along with the Ce^{4+} reduction in the lattice. The doped film presented much higher response (S) values than pure ceria, which demonstrates the higher sensitivity of the doped system to CO. The electrical measurements under different atmospheres revealed a remarkably fast CO response time of 0.9 s for the Eu-doped sample, against 56 s for the pure film, which proves that the introduction of europium cations in the ceria lattice as dopants has a positive effect on the carbon monoxide sensing properties.

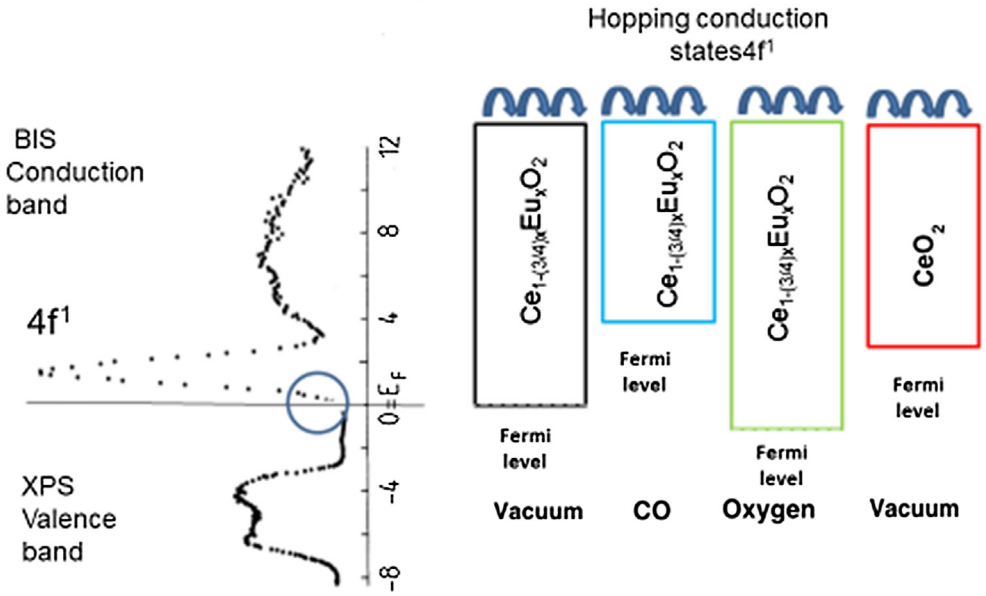

Fig. 9. Band diagram showing the electric conduction mechanism observed for pure and Eu-doped samples.

Acknowledgements

The financial and technical support of this research project by the Brazilian research funding agencies CNPq, CONICET and FAPESP (CEPID 2013/07296-2) is gratefully acknowledged.

References

[1] W. Zhang, D. Chen, Preparation and performance of CeO_2 hollow spheres and nanoparticles, J. Rare Earths 34 (2016) 295–299.
[2] H. He, P. Yang, J. Li, R. Shi, L. Chen, A. Zhang, Y. Zhu, Controllable synthesis, characterization, and CO oxidation activity of CeO_2 nanostructures with various morphologies, Ceram. Int. 42 (2016) 7810–7818.
[3] S. Xie, Z. Wang, F. Cheng, P. Zhang, W. Mai, Y. Tong, Ceria and ceria-based nanostructured materials for photoenergy applications, Nano Energy 34 (2017) 313–337.
[4] Y.C. Wu, C.H. Chien, G. Xu, Conductivity and microstructure analysis of ceria materials doped with multiple elements, Ceram. Int. 43 (2017) S747–S757.
[5] N.M. Zholobak, V.K. Ivanov, A.B. Shcherbakov, A.S. Shaporev, O.S. Polezhaeva, A.Ye. Baranchikov, N.Ya. Spikav, Yu.D. Tretyakov, UV-shielding property, photocatalytic activity and photocytotoxicity of ceria colloid solutions, J. Photochem. Photobiol. B 102 (2011) 32–38.
[6] S. Babu, J.H. Cho, J.M. Dowding, E. Heckert, C. Komanski, S. Das, J. Colon, C.H. Baker, M. Bass, W.T. Self, S. Seal, Multicolored redox active upconverter cerium oxide nanoparticle for bio-imaging and therapeutics, Chem. Commun. 46 (2010) 6915–6917.
[7] X. Wang, J.A. Rodriguez, J.C. Hanson, D. Gamarra, A. Martínez-Arias, M. Fernández-García, In situ studies of the active sites for the water gas shift reaction over Cu-CeO_2 catalysts: complex interaction between metallic copper and oxygen vacancies of ceria, J. Phys. Chem. B 110 (2006) 428–434.
[8] R.C. Deus, R.A.C. Amoresi, P.M. Desimone, F. Schipani, L.S.R. Rocha, M.A. Ponce, A.Z. Simões, E. Longo, Electrical behavior of cerium dioxide films exposed to different gases atmospheres, Ceram. Int. 42 (2016) 15023–15029.
[9] S. Hosokawa, K. Shimamura, M. Inoue, Solvothermal synthesis of ceria nanoparticles with large surface areas, Mater. Res. Bull. 46 (2011) 1928–1932.
[10] Y. Chen, Y. Chen, P. Hu, S. Ma, Y. Li, The effects of PVP surfactant in the direct and indirect hydrothermal synthesis processes of ceria nanostructures, Ceram. Int. 42 (2016) 18516–18520.
[11] A. Zarkov, A. Stanulis, T. Salkus, A. Kezionis, V. Jasulaitiene, R. Ramanauskas, S. Tautkus, A. Kareiva, Synthesis of nanocrystalline gadolinium doped ceria via sol–gel combustion and sol–gel synthesis routes, Ceram. Int. 42 (2016) 3972–3988.
[12] P. Patil, D. Selvakumar, N.S. Kumar, Size controlled preparation and effect of sintering temperature on the structural properties of nanocrystalline Ceria-Lanthana solid solution, Mater. Today-Proc. 3 (2016) 1712–1717.
[13] D.V. Pinjari, A.B. Pandit, Room temperature synthesis of crystalline CeO_2 nanopowder: advantage of sonochemical method over conventional method, Ultrason. Sonochem. 18 (2011) 1118–1123.
[14] C. Tiseanu, V.I. Parvulescu, M. Boutonnet, B. Cojocaru, P.A. Primus, C.M. Teodorescu, C. Solans, M.S. Dominguez, Surface versus volume effects in luminescent ceria nanocrystals synthesized by an oil-in-water microemulsion method, Phys. Chem. Chem. Phys. 13 (2011) 17135–17145.
[15] R.O. Fuentes, R.T. Baker, Structural, morphological and electrical properties of $Ce_{0.9}Gd_{0.1}O_{1.95}$ prepared by a citrate complexation method, J. Power Sources 186 (2009) 268–277.
[16] L.D. Jadhav, M.G. Chourashiya, K.M. Subhedar, A.K. Tyagi, J.Y. Patil, Synthesis of nanocrystalline Gd doped ceria by combustion technique, J. Alloys Compd. 470 (2009) 383–386.
[17] A. Arabaci, M.F. Öksüzömer, Preparation and characterization of 10 mol% Gd doped CeO_2 (GDC) electrolyte for SOFC applications, Ceram. Int. 38 (2012) 6509–6515.
[18] H. Wang, J.J. Zhu, J.M. Zhu, X.H. Liao, S. Xu, T. Ding, H.Y. Chen, Preparation of nanocrystalline ceria particles by sonochemical and microwave assisted heating methods, Phys. Chem. Chem. Phys. 4 (2002) 3794–3799.
[19] H.M. Yang, C.H. Huang, A.D. Tang, X.C. Zhang, W.G. Yang, Microwave-assisted synthesis of ceria nanoparticles, Mater. Res. Bull. 40 (2005) 1690–1695.
[20] M.M. Natile, G. Boccaletti, A. Glisenti, Properties and reactivity of nanostructured CeO_2 powders: comparison among two synthesis procedures, Chem. Mater. 17 (2005) 6272–6286.
[21] A. Mirzaei, G. Neri, Microwave-assisted synthesis of metal oxide nanostructures for gas sensing application: a review, Sensor. Actuat. B-Chem. 237 (2016) 749–775.
[22] B.I. Kharisov, O.V. Kharissova, U.O. Méndez, Microwave Hydrothermal and Solvothermal Processing of Materials and Compounds, in: W. Cao (Ed.), The Development and Application of Microwave Heating, IntechOpen, 2012, pp. 107–140.
[23] M.P. Kalamuei, S. Alizadeh, M.M. Kamazani, M.S. Niasari, Synthesis and characterization of CeO_2 nanoparticles via hydrothermal route, J. Ind. Eng. Chem. 21 (2015) 1301–1305.
[24] G. Shen, Q. Wang, Z. Wang, Y. Chen, Hydrothermal synthesis of CeO_2 nano-octahedrons, Mater. Lett. 65 (2011) 1211–1214.
[25] A.I.Y. Tok, F.Y.C. Boey, Z. Dong, X.L. Sun, Hydrothermal synthesis of CeO_2 nanoparticles, J. Mater. Process. Tech. 190 (2007) 217–222.
[26] C. Wang, L. Yin, L. Zhang, D. Xiang, R. Gao, Metal oxide gas sensors: sensitivity and influencing factors, Sensors 10 (2010) 2088–2106.
[27] R.C. Deus, M. Cilense, C.R. Foschini, M.A. Ramirez, E. Longo, A.Z. Simoes, Influence of mineralizer agents on the growth of crystalline CeO_2 nanospheres by the microwave-hydrothermal method, J. Alloys Compd. 550 (2013) 245–251.
[28] A. Phuruangrat, S. Thongtem, T. Thongtem, Microwave-assisted hydrothermal synthesis and characterization of CeO_2 nanowires for using as a photocatalytic material, Mater. Lett. 196 (2017) 61–63.
[29] A.C. Cabral, L.S. Cavalcante, R.C. Deus, E. Longo, A.Z. Simoes, F. Moura, Photoluminescence properties of praseodymium doped cerium oxide nanocrystals, Ceram. Int. 40 (2014) 4445–4453.
[30] S. Gangopadhyay, D.D. Frolov, A.E. Masunov, S. Seal, Structure and properties of cerium oxides in bulk and nanoparticulate forms, J. Alloys Compd. 584 (2014) 199–208.
[31] J.C. Muñoz, F.A. Prado, J.E.R. Páez, Cerium oxide nanoparticles: Synthesis, characterization and tentative mechanism of particle formation, Colloid. Surface. A 529 (2017) 146–159.
[32] W.Y. Hernández, O.H. Laguna, M.A. Centeno, J.A. Odriozola, Structural and catalytic properties of lanthanide (La, Eu, Gd) doped ceria, J. Solid State Chem. 184 (2011) 3014–3020.
[33] M. Fleischer, M. Lehmann, Solid State Gas Sensors – Industrial Application, Springer, 2012.
[34] A. Mirzaei, S. Park, H.J. Kheel, G.J. Sun, S. Lee, C. Lee, ZnO-capped nanorod gas sensors, Ceram. Int. 42 (2016) 6187–6197.
[35] N. Barsan, U. Weimar, Conduction model of metal oxide gas sensors, J.

Electroceram. 7 (2001) 143–167.
[36] M. Batzill, U. Diebold, The surface and materials science of tin oxide, Prog. Surf. Sci. 79 (2005) 47–154.
[37] L. Zhu, W. Zeng, Room-temperature gas sensing of ZnO-based gas sensor: a review, Sensor. Actuat. A-Phys. 267 (2017) 242–261.
[38] R.C. Deus, C.R. Foschini, B. Spitova, F. Moura, E. Longo, A.Z. Simões, Effect of soaking time on the photoluminescence properties of cerium oxide nanoparticles, Ceram. Int. 40 (2014) 1–9.
[39] R.C. Deus, J.A. Cortés, M.A. Ramirez, M.A. Ponce, J. Andres, L.S.R. Rocha, E. Longo, A.Z. Simões, Photoluminescence properties of cerium oxide nanoparticles as a function of lanthanum content, Mater. Res. Bull. 70 (2015) 416–423.
[40] L.S.R. Rocha, M. Cilense, M.A. Ponce, C.M. Aldao, L.L. Oliveira, E. Longo, A.Z. Simões, Novel gas sensor with dual response under CO(g) exposure: Optical and electrical stimuli, Physica B 536 (2018) 280–288.
[41] N. Tibaldi, M.A. Ponce, P. Kalafatovich, H. Asencio, M.P. Desimone, A.Z. Simões, L. S.R. Rocha, E. Longo, A Device for the Optoelectronic Characterization of Materials, 2015, Argentina, 2015 0103953.
[42] N. Tibaldi, M.A. Ponce, P. Kalafatovich, H. Asencio, M.P. Desimone, A.Z. Simões, L. S.R. Rocha, E. Longo, A Device for the Optoelectronic Characterization of Materials, 2016, Brazil, 10 2016 028383 3.
[43] D. He, H. Hao, D. Chen, J. Liu, J. Yu, J. Lu, F. Liu, G. Wan, S. He, Y. Luo, Synthesis and application of rare-earth elements (Gd, Sm, and Nd) doped ceria-based solid solutions for methyl mercaptan catalytic decomposition, Catal. Today 281 (2017) 559–565.
[44] M. Jamshidijam, P. Thangaraj, A. Akbari-Fakhrabadi, M.A.N. Galeano, J. Usuba, M.R. Viswanathan, Influence of rare earth (RE = Nd, Y, Pr and Er) doping on the microstructural and optical properties of ceria nanostructures, Ceram. Int. 43 (2017) 5216–5222.
[45] D. Mukherjee, B.G. Rao, B.M. Reddy, CO and soot oxidation activity of doped ceria: influence of dopants, Appl. Catal. B-Environ. 197 (2016) 105–115.
[46] J.M. López, A.L. Gilbank, T. García, B. Solsona, S. Agouram, L. Torrente-Murciano, The prevalence of surface oxygen vacancies over the mobility of bulk oxygen in nanostructured ceria for the total toluene oxidation, Appl. Catal. B-Environ. 174–175 (2015) 403–412.
[47] B. Matovic, D. Nikolic, N. Labus, S. Ilic, V. Maksimovic, J. Lukovic, D. Bucevac, Preparation and properties of porous, biomorphic, ceria ceramics for immobilization of Sr isotopes, Ceram. Int. 39 (2013) 9645–9649.
[48] E. Wuilloud, B. Delley, W.D. Schneider, Y. Baer, Spectroscopic evidence for localized and extended f-symmetry states in CeO_2, Phys. Rev. Lett. 53 (1984) 202–205.
[49] H. Li, F. Meng, J. Gong, Z. Fan, R. Qin, Structural, morphological and optical properties of shuttle-like CeO_2 synthesized by a facile hydrothermal method, J. Alloy Compd. 722 (2017) 489–498.
[50] P.C.A. Brito, D.A.A. Santos, J.G.S. Duque, M.A. Macedo, Structural and magnetic study of Fe-doped CeO_2, Physica B 405 (2010) 1821–1825.
[51] E. Shi, C.T. Xia, W.Z. Zhong, B.G. Wang, C.D. Feng, Crystallographic properties of hydrothermal barium titanate crystallites, J. Am. Ceram. Soc. 80 (1997) 1567–1572.
[52] H.L. Tuller, A.S. Nowick, Small polaron electron transport in reduced CeO_2 single crystals, J. Phys. Chem. Solids 38 (1977) 859–867.
[53] G.V.S. Rao, S. Ramdas, P.N. Mehrotra, C.N.R. Rao, Electrical transport in rare-earth oxides, J. Solid State Chem. 2 (1970) 377–384.
[54] L. Zhang, J. Zhao, J. Zheng, Z.Z. Zhu, Hydrothermal synthesis of hierarchical nanoparticle-decorated ZnO microdisks and the structure enhanced acetylene sensing properties at high temperatures, Sensor. Actuat. B-Chem. 158 (2011) 144–150.
[55] C.M. Ghimbeu, J. Schoonman, M. Lumbreras, M. Siadat, Electrostatic spray deposited zinc oxide films for gas sensor applications, Appl. Surf. Sci. 253 (2007) 7483–7489.
[56] H. Gong, J.Q. Hu, J.H. Wang, C.H. Ong, F.R. Zhu, Nano-crystalline Cu-doped ZnO thin film gas sensor for CO, Sens. Actuat. B-Chem. 115 (2006) 247–251.
[57] S.M.A. Durrani, M.F. Al-Kuhaili, I.A. Bakhtiari, Carbon monoxide gas-sensing properties of electron-beam deposited cerium oxide thin films, Sensor. Actuat. B-Chem. 134 (2008) 934–939.
[58] T. Itoh, N. Izu, T. Akamatsu, W. Shin, Y. Miki, Y. Hirose, Elimination of flammable gas effects in cerium oxide semiconductor-type resistive oxygen sensors for monitoring low oxygen concentrations, Sensors 15 (2015) 9427–9437.
[59] N. Izu, S. Nishizaki, T. Itoh, M. Nishibori, W. Shin, I. Matsubara, Gas response, response time and selectivity of a resistive CO sensor based on two connected CeO_2 thick films with various particle sizes, Sensor. Actuat. B-Chem. 136 (2009) 364–370.
[60] E.R.L. Mena, C.R. Michel, A.H.M. Preciado, A.E. Zuñiga, Simple route to obtain nanostructured CeO_2 microspheres and CO gas sensing performance, Nanoscale Res. Lett. 12 (2017) 169.
[61] N. Izu, I. Matsubara, T. Itoh, T. Akamatsu, W. Shin, CO responses of sensors based on cerium oxide thick films prepared from clustered spherical nanoparticles, Sensors 13 (2013) 3252–3261.